Article

Direct observation of chemical short-range order in a medium-entropy alloy

https://doi.org/10.1038/s41586-021-03428-z

Received: 27 September 2020

Accepted: 8 March 2021

Published online: 28 April 2021

Check for updates

Xuefei Chen[1,2,7], Qi Wang[3,7], Zhiying Cheng[4,7], Mingliu Zhu[1], Hao Zhou[5], Ping Jiang[1], Lingling Zhou[1,2], Qiqi Xue[1,2], Fuping Yuan[1,2], Jing Zhu[4]✉, Xiaolei Wu[1,2]✉ & En Ma[6]✉

Complex concentrated solutions of multiple principal elements are being widely investigated as high- or medium-entropy alloys (HEAs or MEAs)[1–11], often assuming that these materials have the high configurational entropy of an ideal solution. However, enthalpic interactions among constituent elements are also expected at normal temperatures, resulting in various degrees of local chemical order[12–22]. Of the local chemical orders that can develop, chemical short-range order (CSRO) is arguably the most difficult to decipher and firm evidence of CSRO in these materials has been missing thus far[16,22]. Here we discover that, using an appropriate zone axis, micro/nanobeam diffraction, together with atomic-resolution imaging and chemical mapping via transmission electron microscopy, can explicitly reveal CSRO in a face-centred-cubic VCoNi concentrated solution. Our complementary suite of tools provides concrete information about the degree/extent of CSRO, atomic packing configuration and preferential occupancy of neighbouring lattice planes/sites by chemical species. Modelling of the CSRO order parameters and pair correlations over the nearest atomic shells indicates that the CSRO originates from the nearest-neighbour preference towards unlike (V–Co and V–Ni) pairs and avoidance of V–V pairs. Our findings offer a way of identifying CSRO in concentrated solution alloys. We also use atomic strain mapping to demonstrate the dislocation interactions enhanced by the CSROs, clarifying the effects of these CSROs on plasticity mechanisms and mechanical properties upon deformation.

We selected V-Co-Ni as a model system, because the equilibrium V–Co, V–Ni and V–Co–Ni phase diagrams[23,24] show binary and ternary intermetallic compounds over a range of temperatures and compositions. The VCoNi MEA, previously claimed to be a face-centred-cubic (fcc) random solid solution at room temperature[23], is therefore a metastable phase with a high likelihood of partial chemical order. Specifically, we hypothesize that this single-phase fcc MEA has a preference for V–Co and V–Ni bonds accompanied by V–V avoidance. Such CSROs, however, are notoriously difficult to observe in a direct manner[12–22]. We therefore designed systematic and meticulous experiments to avoid the need for data fitting[17] and/or multiple possible interpretations[22]. The complementary characterization tools we chose are described in the Methods. The transmission electron microscope (TEM) observations, as displayed in Fig. 1a, shows a dual-phase microstructure in the VCoNi MEA. The dominant phase is the fcc solution, at a volume fraction of about 80%. The minority phase, occupying about 20% of the sample volume, has a long-range chemically ordered $L1_2$ structure, residing as plates inside the fcc grains and containing a high density of faults. The fully recrystallized fcc solution (see Methods) is composed of equi-axed and dislocation-free grains, with an average size of 1.2 μm. Its composition, from atom probe tomography data (not shown), is $V_{36}Co_{33}Ni_{31}$, slightly shifted relative to the overall VCoNi composition, owing to the coexisting $L1_2$, which contains a little more Co and Ni. From here on, we will focus on the fcc solution only, to locate and dissect the CSROs that emerge inside this single phase. Figure 1b presents the lattice image of this fcc phase. The selected-area electron diffraction pattern (EDP) (left inset, lower right corner in Fig. 1a) and nano beam EDP (right inset in Fig. 1a), together with the fast Fourier transform (FFT) pattern (inset in Fig. 1b), show no additional diffraction information beyond the normal fcc Bragg spots. No CSRO could be detected from these results under the [110] zone axis, which has been normally used in previous TEM work[22].

Dramatic differences emerge when the [112] zone axis was adopted, as shown in Fig. 2 (for a sample after tensile pulling to 18% plastic strain, but the sample before deformation (Extended Data Fig. 1) gives very similar results). Figure 2a is the selected-area EDP of one fcc grain, showing the expected fcc spots. Interestingly, there are extra disks, which are highly diffuse but visible halfway in between the transmission spot (000) and the $\{\bar{3}11\}$ spots; one example is highlighted using a yellow circle. These extra diffuse disks in reciprocal space, each with a diameter several times that of the normal Bragg spot, are definitive indications that there exists additional order in real space that must

[1]State Key Laboratory of Nonlinear Mechanics, Institute of Mechanics, Chinese Academy of Sciences, Beijing, China. [2]School of Engineering Science, University of Chinese Academy of Sciences, Beijing, China. [3]Science and Technology on Surface Physics and Chemistry Laboratory, Jiangyou, China. [4]National Center of Electron Microscopy in Beijing, School of Materials Science and Engineering, Tsinghua University, Beijing, China. [5]Nano and Heterogeneous Materials Center, School of Materials Science and Engineering, Nanjing University of Science and Technology, Nanjing, China. [6]Center for Alloy Innovation and Design (CAID), State Key Laboratory for Mechanical Behavior of Materials, Xi'an Jiaotong University, Xi'an, China. [7]These authors contributed equally: Xuefei Chen, Qi Wang, Zhiying Cheng. ✉e-mail: jzhu@tsinghua.edu.cn; xlwu@imech.ac.cn; maen@xjtu.edu.cn

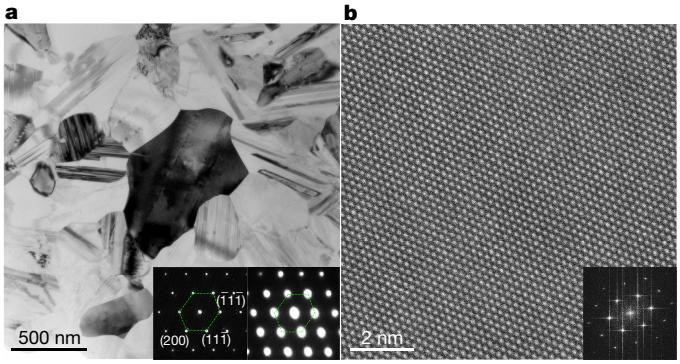

Fig. 1 | TEM microstructure of VCoNi MEA. Both images were taken with the [110] zone axis for the fcc phase. **a**, Bright-field TEM image showing the equi-axed, dislocation-free fcc grains, with faulted $L1_2$ plates inside, in the as-prepared microstructure after cold rolling followed by recrystallization annealing at 1,173 K. Left and right insets show the selected-area EDP and nano-beam EDP, respectively. **b**, Lattice image of the fcc solution and the corresponding FFT pattern (inset).

be very small in spatial extent[25–28]. To improve the signal-to-noise (background) ratio, we further carried out nano-beam (about 35 nm in diameter) EDP, using the same [112] zone axis. This led to much better contrast (Fig. 2b): the extra reflections are easily discernible. These disks all line up at the positions corresponding to $\frac{1}{2}\{\bar{3}11\}$, as marked using arrows, clearly indicating the presence of CSRO. To observe the locations and dimensions of coherently diffracting regions, Fig. 2c shows the dark-field TEM image (with a close-up view in the inset) taken using the extra reflections; the vast majority (90%) of these CSRO regions that light up are less than 1 nm in size, with an average size $\bar{d} \approx 0.6$ nm; see the size distribution in Fig. 2d (and Extended Data Fig. 1a-3). The CSRO regions take up around 25% of the total area in these images.

Figure 2e is the high-angle annular dark-field (HAADF) lattice image of the fcc phase, and the inset is the corresponding FFT pattern ([112] zone axis. Extra diffuse reflections (one is circled in yellow) are again observed in addition to the fcc diffraction spots (blue circles). Using these, inverse FFT images are obtained: the CSRO regions light up inside the yellow circles in Fig. 2f, and the corresponding image for the normal fcc lattice is in Fig. 2g. Superimposing the two images leads to Fig. 2h, with details in the close-up view in the inset. In this overlapped image, the CSRO stands out even more clearly because it adds intensity onto the fcc columns . The red dashed rectangle gives the cell motif corresponding to the local CSRO configuration. Of special note is that the lattice planes (yellow dashed lines) characterizing the CSRO periodicity have an inter-planar spacing (d_{CSRO}) that is twice the inter-planar spacing d_{fcc} of the $\{\bar{3}11\}$ planes in the fcc phase (blue dashed lines), as illustrated in the inset in Fig. 2h. Such chemical order, doubling the d_{fcc}, explains why the superlattice reflections appear at the locations corresponding to $\frac{1}{2}\{\bar{3}11\}$ in Fig. 2a, b and e.

We next wished to determine what kind of CSRO is present and why; that is, the detailed arrangements of the three elemental species constituting the CSROs. To this end, we carried out energy-dispersive X-ray spectroscopy (EDS) mapping: see Fig. 3a and additional maps as shown in Extended Data Fig. 2, based on HAADF imaging with the [112] zone axis. In Fig. 3a, each spot corresponds to an atomic column along the thickness direction of the TEM foil. We mapped out each element, V (red), Co (green) and Ni (blue), one by one. The intensity (brightness) of the coloured spot depends on the make-up of the column, scaling with the content of the particular element being probed. We discover that the CSRO can be best described in terms of the V occupancy. Specifically, as seen in the EDS maps (two examples are shown, respectively, in the left and right columns in Fig. 3b), two V-enriched $(\bar{3}11)$ planes (see the map for V, under dashed yellow lines, across the red spots) sandwich one V-depleted $(\bar{3}11)$ plane (in either the V–Co or V–Ni map, under dashed blue line, across the intense green/blue spots but with faint or even vanishing red V). In other words, the V-enriched $(\bar{3}11)$ planes alternate with those enriched in Co and/or Ni. This alternating

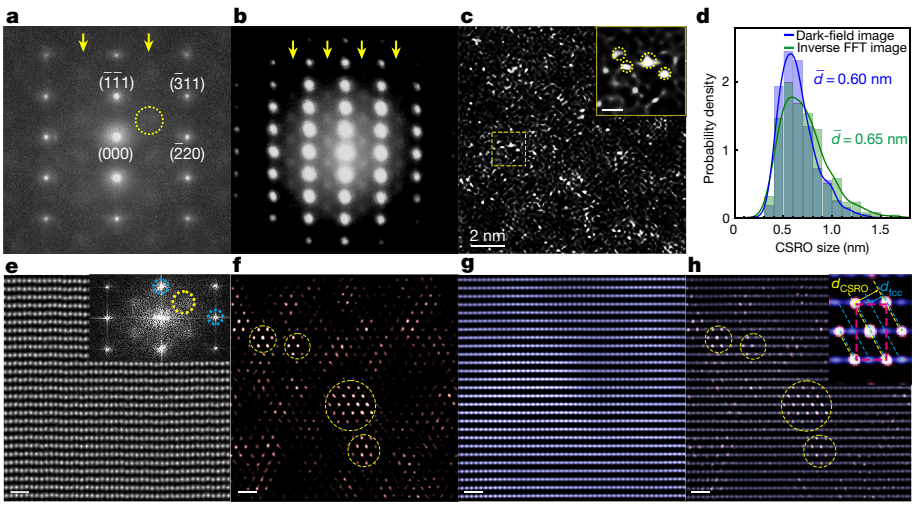

Fig. 2 | Evidence of CSRO in the fcc VCoNi. The sample was deformed in tension to 18% plastic strain. **a**, Selected-area EDP with the [112] zone axis. We note two arrays of extra and diffuse disks (indicated by arrows) appearing at $\frac{1}{2}\{\bar{3}11\}$ positions (one example is inside the yellow circle). **b**, Nano-beam EDP with the [112] zone axis. Arrays of superlattice reflections at $\frac{1}{2}\{\bar{3}11\}$ positions as indicated by arrows. **c**, Energy-filtered dark-field TEM image taken using the diffuse reflections, with the inset showing a close-up view of the dashed square area, highlighting some coherently diffracting clusters corresponding to the local CSROs. The size distribution of these CSRO regions is shown in **d**. The average size $\bar{d}$ is 0.60 nm and 0.65 nm, based on the dark-field TEM image and the inverse FFT image, respectively. **e**, Lattice image of the fcc phase with the [112] zone axis and the corresponding FFT pattern (inset). This pattern again displays the extra diffuse reflections (see, for example, inside the yellow circle) at $\frac{1}{2}\{\bar{3}11\}$ positions, besides the sharper Braggs spots from the fcc phase (blue circles). **f**, **g**, Inverse FFT image showing the CSRO regions (several are circled), and the fcc lattice, respectively. These two images are superimposed in **h**, with a close-up view of a CSRO region in the inset. Overlapping in this way produces bright sites that highlight the extra CSRO lining up on $\{\bar{3}11\}$ planes (yellow dashed lines). d_{fcc} denotes the spacing of $\{\bar{3}11\}$ planes in the normal fcc lattice, whereas d_{CSRO} displays the spacing corresponding to the extra chemical order. The red dashed box outlines this unit period for the local CSRO configuration. All scale bars are 0.5 nm except in **c**.

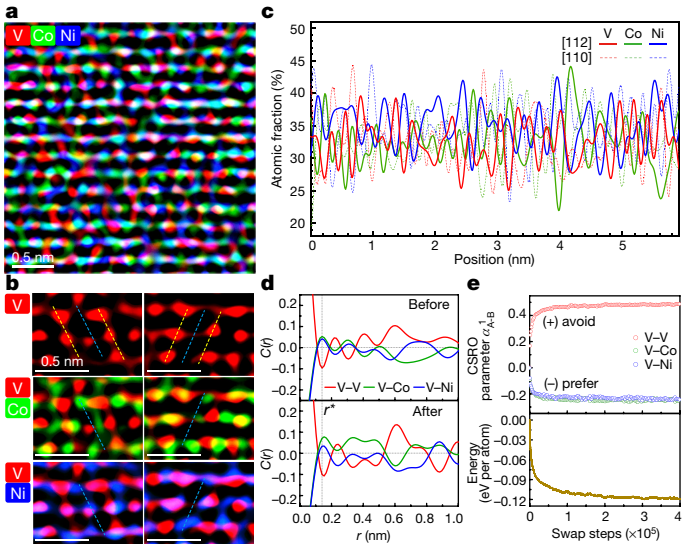

Fig. 3 | Chemical mapping indicating element-specific enrichment on alternating atomic planes. a, EDS maps showing element distribution, atomic column by atomic column, from the HAADF image with the [112] zone axis (Fig. 2e). **b**, Close-up maps of V, V-Co, and V-Ni, respectively, in two local regions in **a** (see Extended Data Fig. 2 for additional maps showing the distribution of Co, Ni and Co+Ni). All dashed lines mark the $(\bar{3}11)$ planes intersecting the $(11\bar{1})$ plane in plan view: yellow: V-enriched, blue: Co-/Ni-enriched. All scale bars are 0.5 nm. **c**, Line scan profiles along the horizontal direction. Each line profile represents the distribution of an element in a (111) plane, column by column, projected along either the [110] or the [112] zone axis. **d**, Pair correlation coefficients, $C_{A\text{-}B}(r)$, calculated from 17 experimental EDS line profiles, are plotted over a spatial distance on the short-to-medium range length scale to quantitatively gauge the CSRO. The correlation and anti-correlation of chemical species are obvious (see text), and similar before and after tensile straining. **e**, Evolution of the Warren–Cowley short-range order parameter α^1_{A-B} indicates the development of V–V, V–Co and V–Ni CSRO (upper panel). The steadily reducing energy (lower panel) with increasing swap Monte Carlo steps underscores the origin of the CSRO.

chemical occupancy extends across only a few $(\bar{3}11)$ planes, that is, a distance of less than 1 nm, and can hence be rightfully classified as chemical short-to-medium range order. Again, the two V-enriched planes are separated by a distance twice the normal spacing of $\{\bar{3}11\}$ planes in the fcc lattice, as there is one Co/Ni-enriched plane in between. As a result, extra reflections appear at the $\frac{1}{2}\{\bar{3}11\}$ positions in Fig. 2b, e.

We also monitored the spatial distribution of each individual element from column to column along the horizontal ($[\bar{1}10]$) direction in Fig. 3a. The atomic fraction, an average for each atomic column, is plotted in Fig. 3c. The atomic concentration (percentage) of V, Co and Ni varies from one atomic column to another, although on average the chemical composition from the local chemical maps is not far from the global fcc composition, $V_{36}Co_{33}Ni_{31}$. Although the EDS profile in Fig. 3c is useful for observing compositional fluctuation[21], it is necessary to devise a powerful metric with which to quantify the spatial correlations of chemical species. To this end, we calculate a set of pair correlation coefficients, $C_{A\text{-}B}(r)$ (see definition, test and feature details in Supplementary Information sections 1 and 2), to gauge the strength of positive and negative self-correlation or cross-correlation of the species at r over short-to-medium range in our one-dimensional line profiles. We monitored 17 independent EDS line profiles. Figure 3d shows the correlation coefficient for V–V, V–Co and V–Ni at various r values up to 1.0 nm. We observe an obvious $C_{A\text{-}B}(r)$ peak/valley at r^* (around 0.14 nm); see Extended Data Fig. 3a for a schematic showing the direct correspondence between this r^* and the (1st) nearest neighbour CSRO. To be specific, while V–Co and V–Ni exhibit positive $C(r^*)$, preferring to be (1st) nearest neighbours, V–V tend to avoid each other, showing a negative $C(r^*)$. In fact, the strength of correlation indicated by the absolute $C(r^*)$ values—that is, V–V being approximately two times V–Co and V–Ni whereas V–Co is slightly larger than V–Ni—is also in agreement with the degree of CSRO in the upper panel of Fig. 3e, which is the theoretically predicted magnitude for the order parameter (see below). Meanwhile, negative and positive $C(r^*)$ values alternate, persisting roughly (due to lattice-distortion-induced displacement/uncertainty especially at large separation distances) at 2, 3 and 4 times the distance r^*. That is, the correlation (together with concurrent anti-correlation) suggests a repeating CSRO pattern across several neighbouring atomic columns: Co(Ni)-enriched, V-enriched, Co(Ni)-enriched, V-enriched and so on, both before (upper panel in Fig. 3d) and after (lower panel in Fig. 3d) tensile deformation. This alternating neighbouring-column chemical preference in the (111) planes indicates the same preference/avoidance trend as our observations about the (311) type planes (Figs. 2h, 3b). The thermodynamic driving force leading to the CSRO is shown in the lower panel of Fig. 3e, which will be discussed later (and in Supplementary Information section 3).

Next, in Extended Data Fig. 4 we use schematics to help visualize the local three-dimensional atomic configuration that corresponds to the CSRO identified above. The inverse FFT image (Fig. 2h and inset) and EDS mapping (Fig. 3b) suggest that V atoms have a tendency/preference to occupy the eight vertices of the unit cell, interspersed with Co/Ni-enriched positions along the [111] direction. This is idealized in the model in Extended Data Fig. 4a, viewed from the [112] zone axis. This simplified model captures the alternating $\{\bar{3}11\}$ planes (red ball planes interspersed with blue ball planes)—the salient chemical enrichment repeatedly featured in figures such as Fig. 2h and its inset, as well as the peak/valley undulation along $[\bar{1}10]$ scan direction in Fig. 3. An idealized three-dimensional local configuration that corresponds to the CSRO can thus be hypothesized in Extended Data Fig. 4b (to be analysed elsewhere). The EDP corresponding with the [112] zone axis in Extended Data Fig. 4c shows the extra diffuse disks at the $\frac{1}{2}\{\bar{3}11\}$ positions, in full agreement with direct experimental observations in Figs. 2a, b, e. Therefore, it is such an atomic configuration/arrangement that locally breaks the fcc symmetry to produce the extra reflections, while all V, Co and Ni atoms reside on the fcc lattice sites.

In the following discussion, we make four important points that are of interest to the HEA/MEA community. First, we carried out density functional theory (DFT)-based modelling to monitor the evolution of CSRO and understand the underlying energetics. See Methods for the methodology[29–32] we adopted. The cohesive energy gradually and substantially decreases with ordering (Fig. 3e). This demonstrates the thermodynamic driving force responsible for the CSRO observed. Meanwhile, we track the CSRO using the Warren–Cowley order parameter α^s_{A-B}, where subscript 'A-B' indicates the pair consisting of element A and element B in the sth nearest-neighbour shell (Fig. 3e, see Methods). We see that VCoNi is not random ($\alpha^s_{A-B} \approx 0$), but instead strongly disfavours V–V connection in the 1st-neighbour shell, as indicated by the positive α^1_{V-V}, and prefers V–Co and V–Ni (negative α^1_{V-Co} or α^1_{V-Ni}). α^1_{V-V} is about twice the magnitude of α^1_{V-Co} or α^1_{V-Ni}, and V–Co is slightly more favoured than V–Ni (Fig. 3e). These theoretical findings explain the experimentally observed CSRO reported above.

Second, we explain using a simplified model why the CSRO has been difficult to detect in HEAs and MEAs. A projection of the (111) plane along the [110] beam direction is shown in Extended Data Fig. 3b. Suppose that for a given atom (take the blue C as centre), its six (1st) nearest neighbours (and none of its 2nd nearest neighbours) residing in this plane are unlike species, and for simplicity we assume the 3rd and 4th nearest neighbours (grey spheres) have negligible effects. As illustrated, when projecting along the [110] direction (dashed lines in Fig. 3b), the centre is directly superimposed on two 1st neighbours, resulting in a mixed-species column that blurs the difference from other neighbouring columns and hence the contrast in the image and chemical mapping. Previous attempts used only the [100] and [110]

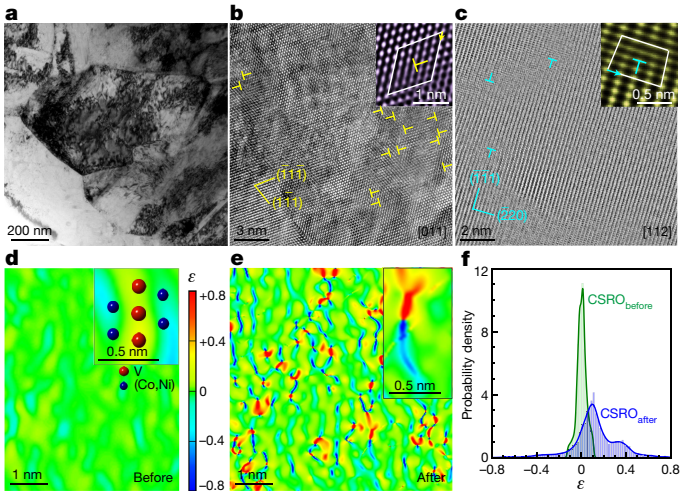

Fig. 4 | Interaction between CSRO regions and dislocations. a, TEM microstructure after tensile deformation, showing stored dislocations. **b**, **c**, Lattice images showing dislocations, with the [110] and [112] zone axis. Insets are Burgers circuits encircling the dislocations (marked by 'T' symbols) identifying Burgers vector $\mathbf{b}=\frac{1}{2}[110]$ and $\mathbf{b}=\frac{1}{3}[111]$, respectively. **d**, **e**, Strain ε mapping before and after tensile deformation calculated from lattice images in the fcc phase with the [110] zone axis. The yellow band of positive strain is induced by a V-enriched column in the CSRO (see inset in **d**). The inset in **e** is a close-up view showing the edge-dislocation-induced strain field: the two coterminous fine fibre-like areas with highly contrasting positive (red) and negative (blue) strain are due to the extra half atomic plane. The dislocation strains overlap with the strains (yellow) due to CSRO. **f**, Upon tensile deformation, the magnitude of the strain around the CSROs increases and its distribution widens.

zone axes[21,22]. As illustrated in Extended Data Fig. 3a, the alternating V-rich and Co (Ni)-rich columns are best visualized with the [112] beam direction.

Third, we observe that the degree of CSRO is almost the same before and after tensile deformation. Before deformation, Extended Data Fig. 1 shows that $\bar{d}=0.6$ (0.62) nm, the areal fraction of CSRO $f_{\text{areal}}=14\%$ (25%), and out of all CSRO regions the fraction of CSRO less than 1 nm = 91% (89%), based on the dark-field image (or inverse FFT image), which are all similar to those in Fig. 2d. It appears that the plastic strain experienced is insufficient to cause marked reduction of CSRO in this ordering-prone alloy. Dislocations may spread to many planes when there is work hardening. Even when repeated dislocation shear on a slip plane would destroy chemical order towards a random mixture[20], CSROs remain intact on other planes.

Fourth, we address how local chemical order influences the mechanical behaviour of HEAs and MEAs[20–22]. Here we probe into one aspect of this issue: the CSROs are expected to interact with moving dislocations. We observed profuse dislocation tangles in the fcc phase, rather than planar slip; see Fig. 4a. The full dislocations (marked by 'T' symbols) exhibit a high density on the order of 3.1×10^{12} cm^{-2}; see lattice image in Fig. 4b. Viewed from the [112] zone axis (Fig. 4c), the immobile Frank dislocations are also plentiful, with a high density of 6.2×10^{11} cm^{-2}. Furthermore, we conducted geometric phase analysis[33] to shed light on the interaction between the CSROs and dislocations (see Methods). Specifically, the geometric phase analysis compares the atomic strain field around the CSRO, to gauge the change incurred by interactions with the dislocations trying to pass by. Figure 4d is the strain map under the [110] zone axis. The dispersed yellow regions (example shown in inset of Fig. 4d) correspond to the CSROs, showing elastic strains due to the relatively large radius of V atoms mismatched with Co and Ni. More details are in Extended Data Fig. 5, showing tensile (positive) strain due to V and compressive (negative) strain nearby. After deformation, the strain map features many slender areas of contrasting local strains (Fig. 4e); the inset shows a typical edge-dislocation-induced strain field. The extra half atomic plane of edge dislocation causes tensile strain above the slip plane (area in red), and compressive strain (area in blue) below. We note that these strain contours around the dislocations frequently reside right on top of those (yellow bands) from the CSRO. This CSRO–dislocation coupling increases the local strain around CSROs (Fig. 4f). This interaction can be understood as follows. An extra force is needed on a moving dislocation when it encounters, and has to break, the energetically favoured CSROs. This entails a trapping effect on the moving dislocations. As a result, the dislocation line migrating through the field of CSRO heterogeneities slows down, and its forward progression has to proceed via local segments cutting through and de-trapping from the local CSROs. This wavy and sluggish process is expected to increase the opportunities for dislocations to interact with one another, leading to tangles and reactions. One would then expect the CSROs to increase strain hardening during tensile deformation.

We conclude that a nominally random multi-principal-element solid solution can contain partial chemical order, even though CSROs are difficult to detect. Our fcc VCoNi provides a dataset that conclusively demonstrates substantial CSRO in a single-phase MEA with a composition near the centre of the phase diagram. Existing engineering alloys typically make use of chemically ordered intermetallics; now, in concentrated solutions such as MEAs/HEAs, we have identified their equivalent—the local chemical orders and their CSRO building blocks. The CSRO can be the same as the chemical order in a known (equilibrium) second phase; it can also be a new metastable order, including a variant/extension of a previously observed order in a related alloy. We note that although CSROs are by definition limited to (sub)nanometre spatial extents, local chemical orders built upon the CSROs can develop to long-range in some of the three dimensions. We have yet to take full advantage of these chemical heterogeneities[5], which provide an opportunity to tune properties in concentrated solutions.

Online content

Any methods, additional references, Nature Research reporting summaries, source data, extended data, supplementary information, acknowledgements, peer review information; details of author contributions and competing interests; and statements of data and code availability are available at https://doi.org/10.1038/s41586-021-03428-z.

1. Ye, Y. F., Wang, Q., Lu, J., Liu, C. T. & Yang, Y. High-entropy alloy: challenges and prospects. *Mater. Today* **19**, 349–362 (2016).
2. Miracle, D. B. & Senkov, O. N. A critical review of high entropy alloys and related concepts. *Acta Mater.* **122**, 448–511 (2017).
3. Wei, S., He, F. & Tasan, C. C. Metastability in high-entropy alloys: a review. *J. Mater. Res.* **33**, 2924–2937 (2018).
4. George, E. P., Raabe, D. & Ritchie, R. O. High-entropy alloys. *Nat. Rev. Mater.* **4**, 515–534 (2019).
5. Ma, E. & Wu, X. L. Tailoring heterogeneities in high-entropy alloys to promote strength–ductility synergy. *Nat. Commun.* **10**, 5623 (2019).
6. George, E. P., Curtin, W. A. & Tasan, C. C. High entropy alloys: a focused review of mechanical properties and deformation mechanisms. *Acta Mater.* **188**, 435–474 (2020).
7. Li, Z., Pradeep, K. G., Deng, Y., Raabe, D. & Tasan, C. C. Metastable high-entropy dual-phase alloys overcome the strength–ductility trade-off. *Nature* **534**, 227–230 (2016).
8. Yang, T. et al. Multicomponent intermetallic nanoparticles and superb mechanical behaviors of complex alloys. *Science* **362**, 933–937 (2018).
9. Lei, Z. et al. Enhanced strength and ductility in a high-entropy alloy via ordered oxygen complexes. *Nature* **563**, 546 (2018).
10. Gludovatz, B. et al. Exceptional damage-tolerance of a medium-entropy alloy CrCoNi at cryogenic temperatures. *Nat. Commun.* **7**, 10602 (2016).
11. Liu, C. T. Atomic ordering and structural transformation in the V-Co-Ni ternary alloys. *Metall. Trans.* **4**, 1743–1753 (1973).
12. Singh, P., Smirnov, A. V. & Johnson, D. D. Atomic short-range order and incipient long-range order in high-entropy alloys. *Phys. Rev. B* **91**, 224204 (2015).
13. Fernández-Caballero, A. et al. Short-range order in high entropy alloys: theoretical formulation and application to Mo-Nb-Ta-V-W system. *J. Phase Equilibria Diffus.* **38**, 391–403 (2017).
14. Jian, W. R. et al. Effects of lattice distortion and chemical short-range order on the mechanisms of deformation in medium entropy alloy CoCrNi. *Acta Mater.* **199**, 352–369 (2020).

15. Ma, Y. et al. Chemical short-range orders and the induced structural transition in high-entropy alloys. *Scr. Mater*. **144**, 64–68 (2018).
16. Yin, B. L., Yoshida, S. H., Tsuji, N. & Curtin, W. A. Yield strength and misfit volumes of NiCoCr and implications for short-range-order. *Nat. Commun*. **11**, 2507 (2020).
17. Zhang, F. X. et al. Local structure and short-range order in a NiCoCr solid solution alloy. *Phys. Rev. Lett*. **118**, 205501 (2017).
18. Oh, H. S. et al. Engineering atomic-level complexity in high-entropy and complex concentrated alloys. *Nat. Commun*. **10**, 2090 (2019).
19. Ding, J., Yu, Q., Asta, M. & Ritchie, R. O. Tunable stacking fault energies by tailoring local chemical order in CrCoNi medium-entropy alloys. *Proc. Natl Acad. Sci. USA* **115**, 8919–8924 (2018).
20. Li, Q. J. et al. Strengthening in multi-principal element alloys with local-chemical-order roughened dislocation pathways. *Nat. Commun*. **10**, 3563 (2019).
21. Ding, Q. et al. Tuning element distribution, structure and properties by composition in high-entropy alloys. *Nature* **574**, 223–227 (2019).
22. Zhang, R. et al. Short-range order and its impact on the CrCoNi medium-entropy alloy. *Nature* **581**, 283–287 (2020).
23. Sohn, S. S. et al. Ultrastrong medium-entropy single-phase alloys designed via severe lattice distortion. *Adv. Mater*. **31**, 1807142 (2019).
24. Sohn, S. S. et al. High-rate superplasticity in an equiatomic medium-entropy VCoNi alloy enabled through dynamic recrystallization of a duplex microstructure of ordered phase. *Acta Mater*. **194**, 106–117 (2020).
25. Williams, D. B. & Carter, C. B. *Transmission Electron Microscopy, A Textbook for Materials Science* (Springer, 2009).
26. Kuwano, N. et al. In situ TEM observation of long range ordering via short range order in Cu_3Pt. *Bull. Mater. Sci*. **22**, 697–700 (1999).
27. Van Tendeloo, G. & Amelinckx, S. The origin of diffuse intensity in electron diffraction patterns. *Phase Transit*. **67**, 101–135 (1998).
28. Van Tendeloo, G. & Amelinckx, S. On a simple method to determine the origin of diffuse scattering in electron diffraction patterns. *Scr. Metall*. **20**, 335–339 (1986).
29. Tibshirani, R. Regression shrinkage and selection via the lasso. *J. R. Stat. Soc*. **58**, 267–288 (1996).
30. Zunger, A. First-principles statistical mechanics of semiconductor alloys and intermetallic compounds. In *Statics and Dynamics of Alloy Phase Transformations* (eds Turchi, P. E. A. & Gonis, A.) 361–419 (Springer, 1994).
31. Tamm, A., Aabloo, A., Klintenberg, M., Stocks, M. & Caro, A. Atomic-scale properties of Ni-based FCC ternary and quaternary alloys. *Acta Mater*. **99**, 307–312 (2015).
32. Zunger, A., Wei, S., Ferreira, L. G. & Bernard, J. E. Special quasirandom structures. *Phys. Rev. Lett*. **65**, 353–356 (1990).
33. Hÿtch, M. Quantitative measurement of displacement and strain fields from HREM micrographs. *Ultramicroscopy* **74**, 131–146 (1998).

Methods

Materials and sample preparation

The VCoNi MEA was produced by arc-melting pure vanadium, cobalt, and nickel (all >99.9% purity) and subsequently casting into a 130-mm-diameter iron mould under an argon atmosphere. To ensure homogeneity, the ingot was re-melted three times and flipped multiple times. The ingot was then hot-forged at 1,423 K to the dimensions of $10 \times 10 \times 50$ mm^3, homogenization-treated in vacuum at 1,373 K for 2 h, followed by quenching in water. The ingot was cold rolled to 90% thickness reduction, and the final cold-rolled sheets with 1.0 mm thickness were annealed at 1,173 K for 150 s for recrystallization. Differential scanning calorimetry scan at a heating rate of about 10 K per minute (similar to that in our heating to 1,173 K) demonstrates that the heat release peaks corresponding to recovery and recrystallization of the fcc phase are both over when the temperature reaches 1,173 K. Tensile specimens were cut along the rolling direction, with a gauge cross-section of 4×1 mm^2 and 15 mm in length. The uniaxial tensile testing was performed using MTS 793 machine at room temperature and a strain rate of 5×10^{-4} s^{-1}.

TEM techniques

The foils for TEM observations were polished to 50 μm, then punched to disks 3 mm in diameter. Perforation by twin-jet electro-polishing was carried out using a solution of 20 vol% perchloric acid and 80 vol% acetic acid, at −15 °C and 50 mA. The thin regions in the TEM specimen used for TEM experiments are about 30 nm in thickness. Atomic-resolution TEM and HAADF scanning transmission electron microscope (STEM) experiments were performed on an aberration-corrected STEM (FEI Titan Cubed Themis G2 300) operated at 300 kV, equipped with a Super-X EDS with four windowless silicon-drift detectors. The experiments used the following aberration coefficients: A1 ≈ 2.09 nm, A2 ≈ 25.7 nm, B2 ≈ 25.3 nm, C3 ≈ 828 nm, A3 ≈ 490 nm, S3 ≈ 98.5 nm, A4 ≈ 2.99 μm, B4 ≈ 6.85 μm, D4 ≈ 4.74 μm, C5 ≈ −188 μm and A5 ≈ 239 μm, ensuring ≤0.06 nm resolution under normal conditions. The nano-beam electron diffraction was performed under the TEM microprobe mode, with the electron-beam spot diameter of 35 nm. The image was obtained using a Flucam-Viewer camera with Sensitivity 6. Quantitative EDS mapping with atomic resolution was conducted on both the samples before and after tensile testing. The count rate was in the range of 180 to 500 counts per second when acquiring atomic-resolution EDS maps. The dwell time was 5 μs per pixel with a map size of 512 × 512 pixels; each EDS mapping took roughly 1 h to reach a high signal-to-noise ratio.

CSRO parameter

We use the Warren–Cowley order parameter[34] $\alpha^s_{A-B} = 1 - p^s_{A-B}/c_B$ to quantify the CSRO in each specific nearest-neighbouring shell. p^s_{A-B} is the fraction of species B in the sth nearest-neighbouring shell around A, and c_B is the nominal concentration of B. Positive (negative) α^s_{A-B} indicates disfavoured (favoured) A–B pairs in the sth-neighbouring shell.

DFT-based modelling

Modelling complements experiments to understand the energetics and monitor the evolution of the ordering in VCoNi. We started with 400 108-atom randomly substituted VCoNi configurations and their DFT-calculated energies, and fitted a surrogate cluster expansion model[29,30] via active learning (that is, adaptive learning; see details in Supplementary Information section 3). We use the model to guide the swap Monte Carlo simulations[20,31] at 1,173 K to optimize a special quasi-random structure (SQS)[32] with 2,592 atoms. With progressive swap Monte Carlo simulations, the energy substantially decreases, gradually evolving to a state about 120 meV per atom lower than the SQS configuration.

Geometric phase analysis

Geometric phase analysis maps out the strain field from high-resolution TEM images, from the variation of the lattice fringes across the image. FFT was performed on the atomic-resolution images from a specific zone axis. In FFT patterns, the Bragg reflections are related to different crystal planes (hkl). A perfect crystal lattice gives rise to sharply peaked frequency components, while the broadening of Bragg reflections is due to the local lattice distortion. In the VCoNi MEA, the V, Co and Ni atoms are mixed. The atomic radii for V, Co and Ni are 1.35 Å, 1.26 Å and 1.24 Å, respectively. The tensile and compressive strains in the normal direction of the close-packed $(11\bar{1})$ planes are caused by the enrichment of the larger V and the smaller Co/Ni atoms, respectively. In practice, we placed a circular Gaussian mask on the reflection of $(11\bar{1})$ to obtain the strain mapping of the close-packed planes. The resolution was set at 0.25 nm to ensure the full display of lattice strain caused by the CSRO.

Data availability

The data generated during and/or analysed during the current study are available from the corresponding author upon reasonable request.

34. Warren, B. E. *X-Ray Diffraction* (Dover Publications, 1990).

Acknowledgements X.W., F.Y. and P.J. were supported by the National Key Research and Development Program of the Ministry of Science and Technology of China (grant numbers 2019YFA0209900 and 2017YFA0204402), the Basic Science Center Program (grant number 11988102), the Natural Science Foundation of China (grant numbers 11972350 and 11890680), and the Chinese Academy of Sciences (grant number XDB22040503). Z.C. and J.Z. were supported by the Basic Science Center Program (grant number 51788104), the National Key Research and Development Program of the Ministry of Science and Technology of China (2016YFB0700402). E.M. thanks Xi'an Jiaotong University for supporting his work at the Center for Alloy Innovation and Design.

Author contributions X.W. and E.M. conceived the ideas and supervised the project together with J.Z. X.C. and H.Z. performed the TEM, FFT and geometric phase analysis work. Q.W. conducted the pair correlation analysis, DFT and Monte Carlo simulations. Z.C. designed and carried out the STEM experiments. P.J. prepared the materials, samples and heat treatments. P.J., L.Z., Q.X., M.Z. and F.Y. conducted tensile testing, electron backscatter diffraction observations, and mechanical behaviour analysis. All authors participated in the discussions. X.W. and E.M. wrote the paper.

Competing interests The authors declare no competing interests.

Additional information

Supplementary information The online version contains supplementary material available at https://doi.org/10.1038/s41586-021-03428-z.

Correspondence and requests for materials should be addressed to J.Z., X.W. or E.M.

Peer review information *Nature* thanks the anonymous reviewers for their contribution to the peer review of this work. Peer reviewer reports are available.

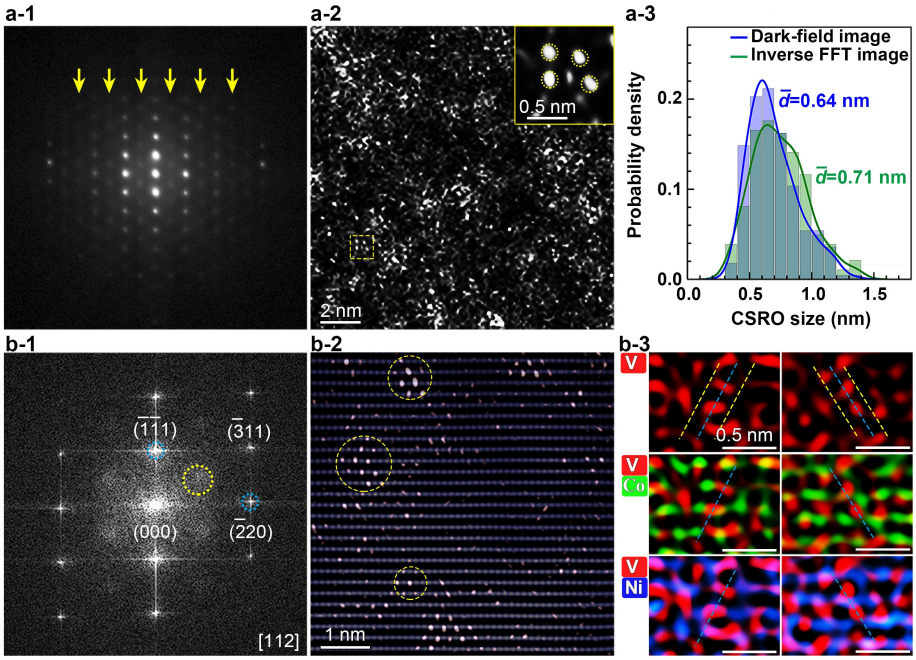

Extended Data Fig. 1 | Evidence of CSRO in the fcc phase of VCoNi MEA before tensile deformation. All results are similar to those after tensile straining shown in Fig. 2. **a-1**, Micro-area EDP with the [112] zone axis. Arrows point to the arrays of superlattice reflections at $\frac{1}{2}\{\bar{3}11\}$ positions. **a-2**, Energy-filtered dark-field TEM image taken using extra reflections. Inset, a close-up view of the area in the dashed-line enclosed square, highlighting an area with CSROs. **a-3**, Statistics showing the size distribution of CSROs, observed in the dark-field TEM images and inverse FFT images. **b-1**, FFT pattern of the fcc phase with the [112] zone axis. The yellow circle highlights a diffuse reflection at $\frac{1}{2}\{\bar{3}11\}$ positions. **b-2**, Inverse FFT image showing the CSROs (circled) that are superimposed on the fcc lattice image. **b-3**, Maps of V, V–Co and V–Ni, respectively, showing two CSROs in two arrays by EDS mapping from the HAADF image with the [112] zone axis in an aberration-corrected TEM. All dashed lines mark the $(\bar{3}11)$ planes intersecting the (111) plane in plan view: yellow: V-enriched, blue: Co-/Ni-enriched. All scale bars are 0.5 nm.

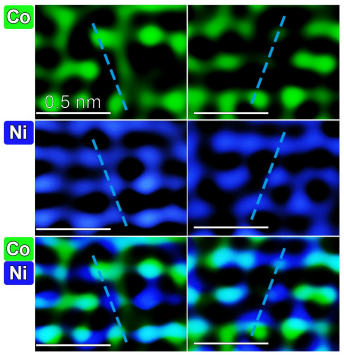

Extended Data Fig. 2 | EDS mapping of the VCoNi alloy with the [112] zone axis. These are additional maps not included in the main text, showing the distribution of Co, Ni and Co+Ni. The dashed lines in each panel mark (Co,Ni)-enriched {311} planes (blue dashed in Fig. 3), which alternate with V-enriched ones.

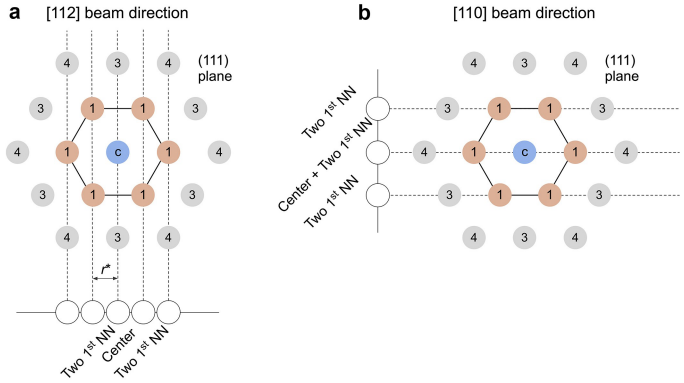

Extended Data Fig. 3 | Illustration of projecting a (111) plane along [112] and [110] beam directions. V–Co(Ni) as the nearest neighbour is assumed in this idealized model to be the prevailing CSRO. The numbers 1, 3 and 4 indicate the 1st, 3rd and 4th nearest neighbours, respectively, around a centre atom C. **a**, Plan view of a close-packed (111) plane, projected along the [112] beam direction. The distance between the nearest points in the [110] direction is r^* (compare with Fig. 3d). **b**, Plan view of the same (111) plane, observed along the [110] beam direction. Unlike for the [112] beam direction, when projected along the [110] beam direction (for example, horizontal dashed lines) the centre atom will be directly superimposed onto two unlike 1st neighbours. This mixed column, when compared with the case in **a** (no overlapping of unlike species in the column) blurs the difference (and hence the contrast) from the neighbouring columns. [112] is therefore the preferred beam direction to see the CSRO of interest.

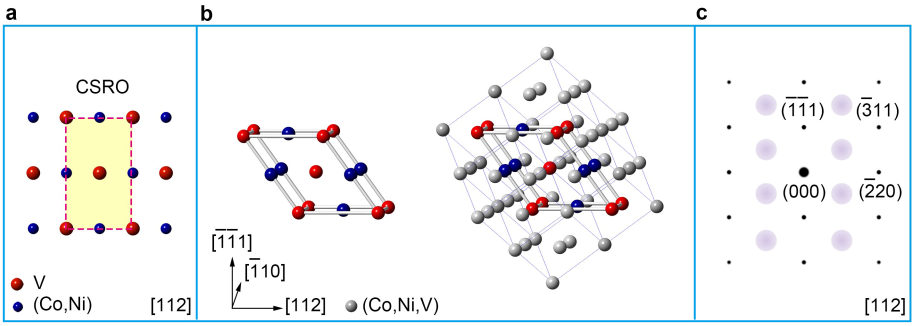

Extended Data Fig. 4 | Schematic of element occupancy that exemplifies the CSRO taking fcc lattice sites. a, Two-dimensional lattice structure of the CSRO, deduced from experimental evidence (the alternating pattern of {311} planes in Fig. 2h and of atomic columns in the {111} plane in Fig. 3d). Note that the red (blue) spheres are meant to represent V (Co,Ni)-enriched atom positions, respectively (i.e., red is not yet V only, but still contains some Co and Ni). The boxed region shows the minimum-sized configuration of the CSRO. **b**, The 3D configuration of the CSRO is based on the motif (left) deduced from observations under both the [112] and [110] z.a. (to be explained in a future publication), and embedded in the fcc matrix (right). Grey spheres indicate random atoms (V,Co,Ni) without chemical order in the fcc lattice. **c**, Simulated diffraction pattern for the sub-nanometre CSRO configuration embedded in the fcc lattice in **b**, with the [112] zone axis, showing the extra reflections at the $\frac{1}{2}\{\bar{3}11\}$ positions (purple diffuse disks).

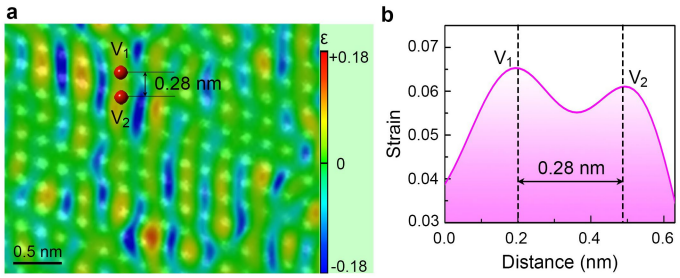

Extended Data Fig. 5 | Strain-field analysis around the CSRO before tensile deformation. a, Geometric phase analysis strain mapping, superimposed on the lattice image taken with the [110] zone axis. The yellow striped areas with positive strain correspond to the CSROs; two red atoms (V_1 and V_2) are displayed to represent the V-enriched columns. **b**, Strain distribution between the two V atoms in **a**. We note that the spacing between the strain peaks of neighbouring V atoms is 0.28 nm. This figure further illustrates the elastic strains observed in Fig. 4. The atomic radii of V, Co, and Ni are 1.35 Å, 1.26 Å and 1.24 Å, respectively. The larger V atoms and the smaller Co/Ni atoms induce tensile and compressive strain, respectively, in the normal direction of close-packed $\{11\bar{1}\}$ planes. The yellow striped bands correspond to the CSROs, with tensile (positive) strain induced by the V-enriched columns in the $(1\bar{1}1)$ plane. Two V atoms (red) are placed in the figure to mark such columns. The strain distribution between these neighbouring columns (V_1 and V_2) is shown in **b**. The spacing between the two strain peaks is 0.28 nm (the average value is 0.3 nm), quite close to the measured spacing between two atomic columns (0.26 nm) based on TEM lattice image. This corroborates that the yellow regions of positive strain are due to the V-enriched columns associated with the CSRO. Nearby regions (blue) experience compressive strain (negative).